

Observing two-electron interactions with correlation-ARPES

A. F. Kemper,^{1,*} Francesco Goto,² Heba A. Labib,¹ Nicolas Gauthier,² E. H. da Silva Neto,^{3,4,5} and F. Boschini^{2,†}

¹*Department of Physics, North Carolina State University, Raleigh, North Carolina 27695, USA*

²*Centre Énergie Matériaux Télécommunications, Institut National de la Recherche Scientifique, Varennes, Québec J3X 1S2, Canada*

³*Department of Physics, Yale University, New Haven, Connecticut 06511, USA*

⁴*Energy Sciences Institute, Yale University, West Haven, Connecticut 06516, USA*

⁵*Department of Applied Physics, Yale University, New Haven, Connecticut 06516, USA*

(Dated: May 6, 2025)

Identifying and studying the underlying two-electron interactions that give rise to emergent phenomena is a key step in developing a holistic understanding of quantum materials. This step is hindered by the lack of an experiment that can directly interrogate the interactions and the specific quasiparticles involved in the interaction simultaneously. We introduce correlation-ARPES (C-ARPES) as a new experimental method that overcomes this difficulty and directly measures the interactions between specific, chosen quasiparticles by measuring the correlations between two electrons photoemitted from the same pulse (but not the same photon). We illustrate how this technique can extract the underlying interactions, and demonstrate this with an example of phonon-mediated electron-electron interactions, such as those that give rise to charge density waves through the Kohn anomaly mechanism.

I. INTRODUCTION

Gaining insight into the many-body interactions between electrons is a central theme in the quest to comprehend quantum materials. Many spectroscopic approaches have been developed and used to characterize and understand the many-body interactions that lead to emergent phenomena. Yet, while condensed matter scientists may dream of one day accessing all possible many-electron correlations in a solid, our understanding of interactions between merely two electrons remains notably limited, as we either observe only the echoes of many-body interactions through their effects on single-particle properties or only catch a glimpse of the interactions in an averaged sense, without being able to resolve details.

Two leading techniques used to study quantum materials today are angle-resolved photoemission spectroscopy (ARPES), a photon-in/electron-out technique that provides direct insight into quasiparticle strength and dispersion in solids [1, 2], and resonant inelastic X-ray scattering (RIXS), an all-optical technique that reveals mechanisms of momentum and energy transfer in the solid[3–7]. These two techniques illustrate the blind spot that exists in our understanding of interactions in a material due to the limitations of the experiments. ARPES measures the properties of electrons in the material as a function of their momentum and energy (k, E). Moreover, the single-particle spectral function probed by ARPES encodes information about the interactions between electrons or with a boson of some sort (emergent or not), characterized by momentum and energy (q, Ω). However, this information is not directly observed in the ARPES

experiment; instead, it must be inferred from the dispersion and linewidth, interpreted through a hypothesized underlying model for the interaction boson [8–16]. On the other hand, RIXS can directly measure the bosonic momentum and energy (q, Ω), but the information is averaged over the various (k, E) electronic quasiparticles involved in the cross-section that generates the bosonic spectral feature[17–19], with a model once again being hypothesized and its parameters adjusted to match the scattering experiment. In both cases, the models are limited in their capacity to account for interaction effects, as they cannot directly capture both quasiparticle (k, ω) and bosonic (q, Ω) degrees of freedom simultaneously. There is thus a clear opportunity for an innovative method capable of directly probing correlations between two quasiparticles of interest — (k_1, E_1) and (k_2, E_2) , and their relative difference ($q = k_2 - k_1, \Omega = E_2 - E_1$) — thus unraveling the electron-electron interactions and overcoming the limitations of ARPES and RIXS.

The development of new experimental methods to directly access the two-electron correlation function Γ_{k_1, k_2} over the entire space of two-electron states $(k_1, E_1, q = k_2 - k_1, \Omega = E_2 - E_1)$ would have a tremendous impact on our understanding of why and under what conditions quantum phases of matter emerge. [Note that in Γ_{k_1, k_2} we are indexing the interaction just by momenta for brevity, dropping the implicit time or energy variable.] An approach to extract both quasiparticle and bosonic information within a single experiment is to build on our established understanding of the photoemission process. For example, the extension of ARPES into the time-domain (time-resolved ARPES [2]) has recently been proposed as a potential approach to extract Γ_{k_1, k_2} . By selectively optically exciting electrons in the surrounding of the (k_1, E_1) electronic state and then tracking their ultrafast direct decay into (k_2, E_2) , Na *et al.* [16] have extracted the mode-projected electron-phonon matrix el-

* akemper@ncsu.edu

† fabio.boschini@inrs.ca

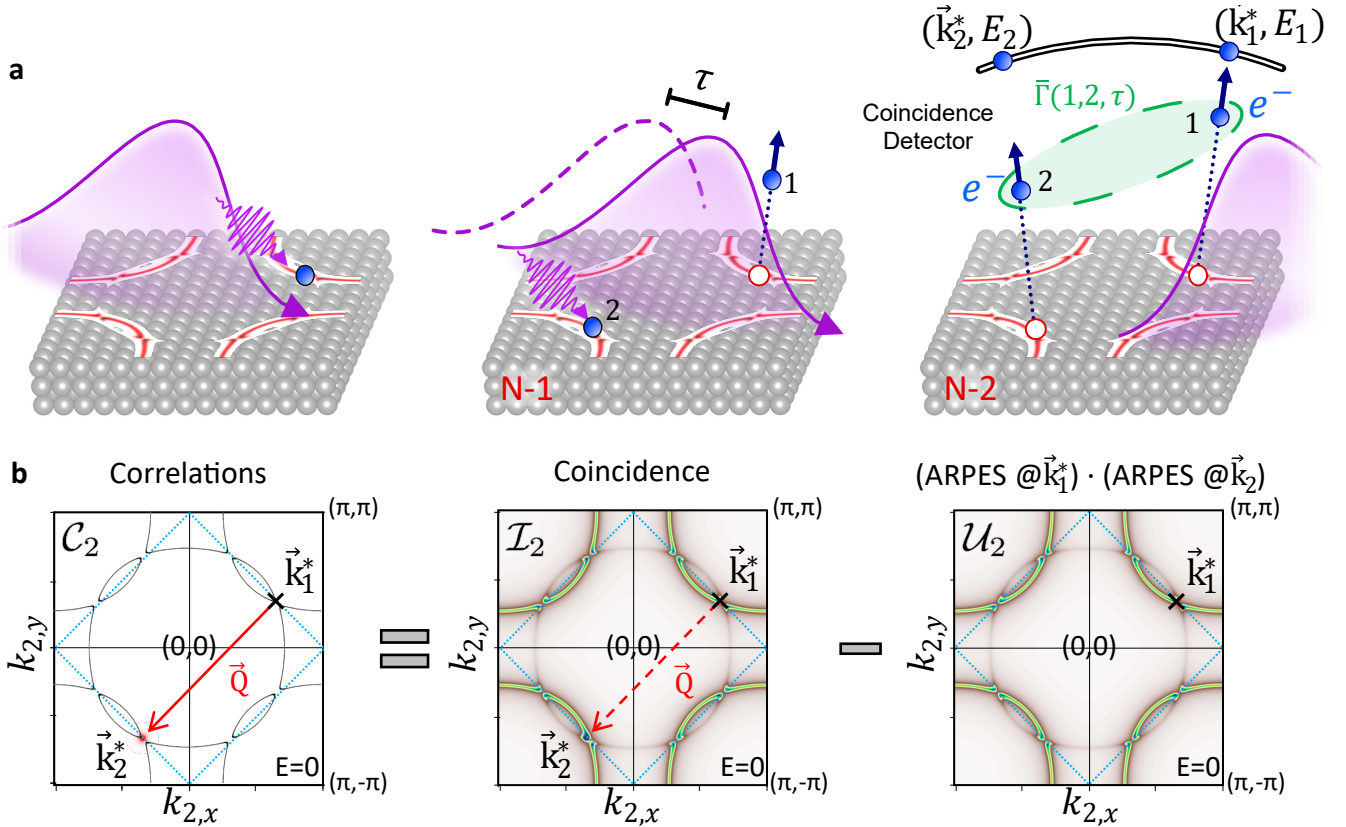


FIG. 1. a) Schematic illustration of the correlation-ARPES (C-ARPES) process. Two electrons are photoemitted between the same pulse, and interactions between them are imprinted on the correlation signal C_2 . b) Correlations (C_2) between the two photoemitted electrons Γ_{k_1,k_2} are obtained by comparing the coincidence (I_2) signal to the one-electron photoemission process (U_2).

ement in graphite. However, although promising, this approach relies heavily on the availability of selective optical transitions, hence limiting its broad applicability.

Another ARPES based approach is to measure the one-photon-in/two-electrons-out process (2e-ARPES), which has been performed in the pioneering work of the research groups of Kirschner, Schumann, and Widdra, demonstrating their potential in uncovering electron correlations in metals[20–28]. When looking at low-energy scales (< 100 meV), 2e-ARPES could also enable direct access to electron interactions responsible for gluing electrons into Cooper pairs[27, 29]. However, the 2e-ARPES cross-section is expected to be much lower compared to a standard ARPES experiment, thereby introducing challenges in its experimental implementation[28, 30, 31].

In this work, we outline how a new technique that we term correlation ARPES (C-ARPES) that can enables a comprehensive mapping of dynamic interactions in quantum materials by directly interrogating the electronic states involved. This method was first introduced by Stahl et al.[32] as a pump-probe coincidence ARPES experiment, who investigated noise-correlations in ARPES and demonstrated the use of this concept in investigating light-quenched superconductivity. As we will show, C-

ARPES is much more general; C-ARPES probes the correlation between two electrons in the solid via the simultaneous detection of two electrons emitted by two photons belonging to the same ultrashort ultraviolet (UV) pulse, as sketched in Fig. 1a. The C-ARPES signal is proportional to the two-particle correlation function between the two quasiparticles and can be visualized in momentum space, Fig. 1b. We show that if an electron with fixed momentum k_1^* is correlated to another electron having momentum k_2^* , the C-ARPES signal $C_2 \propto \Gamma_{k_1^*, k_2^*}$ can be obtained directly by evaluating the difference between the total number of two-electron coincidence events, I_2 , and the uncorrelated part, U_2 (which is proportional to the product between the ARPES intensities of two non-coincident single electrons).

In the following, we discuss the general theoretical framework of C-ARPES, and offer concrete examples. We consider phonon-mediated electron scattering, and illustrate how this type of experiment can reveal the Kohn anomaly that eventually leads to charge density wave formation. We also briefly discuss the use of C-ARPES to study superconductors and charge density waves in the long-range ordered phase.

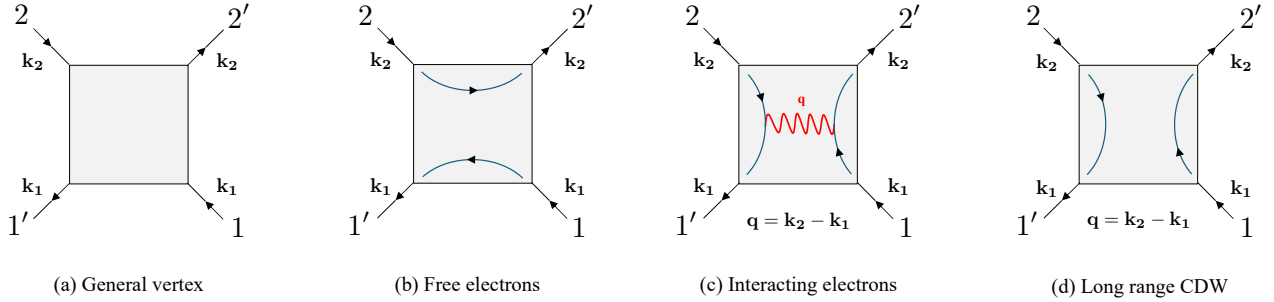


FIG. 2. Feynman diagrams G_2 illustrating the 4-point vertex for the scattering process, where the primed (unprimed) times correspond to annihilation (creation) operators and have been drawn as outgoing (incoming) lines.

II. RESULTS

In this section, we will outline the formalism that underpins the study of C-ARPES, making use of the notation introduced by Stahl et al.[32]. C-ARPES measures the correlation for two coincident free electrons with momenta p and p' , energies E_p and E'_p , and spins σ and σ' :

$$\mathcal{I}_2 = \langle \mathbf{S}^\dagger n_{p\sigma}^f n_{p'\sigma'}^f \mathbf{S} \rangle_0, \quad (1)$$

where \mathbf{S} is the standard time-ordered \mathbf{S} -matrix[33, 34]

$$\mathbf{S} = T_t e^{-i \int_{-\infty}^{\infty} d\bar{t} \mathcal{H}(\bar{t})} \quad (2)$$

and we use the time-loop \mathbf{S} -matrix formalism. For comparison, standard single-electron ARPES signal \mathcal{I}_1 has a single number operator $n_{p\sigma}^f$ in Eq. 1. Here, we will treat the \mathbf{S} -matrix in the interaction representation with respect to two terms:

$$\mathcal{H}(t) = H_{\text{p.e.}}(t) + H_{\text{int}} \quad (3)$$

The first term is responsible for electron emission in the sudden approximation[1, 2, 35],

$$H_{\text{p.e.}} = \sum_{p,k,\sigma,\sigma'} S(t) e^{-i\Omega t} M_{k,p}^{\sigma,\sigma'} c_{k\sigma}^\dagger f_{p\sigma'} + h.c. \quad (4)$$

Here, Ω is the photon energy, $c_{k\sigma}$ and $c_{k\sigma}^\dagger$ are the operators for the electrons in the solid, $f_{p\sigma'}$ and $f_{p\sigma'}^\dagger$ for the free electrons, and $S(t)$ is the probe pulse temporal envelope. $M_{k,p}^{\sigma,\sigma'}$ is the matrix element, which for simplicity we will set to $M \delta_{k,p} \delta_{\sigma,\sigma'}$ (note that we will label the quasiparticles by their crystal momentum k). More complex matrix elements can be readily included, but occlude the notation.

The remaining interaction term depends on the particular interaction that is being considered, *e.g.* electron-electron or electron-phonon scattering, which we will detail below.

A. C-ARPES of free electrons

We first consider the simplest case of free electrons, with $H_{\text{int}} = 0$. A straightforward perturbation theory in $H_{\text{p.e.}}$, considering the initial free electron state to be empty, yields the conclusion that the electron operators appear in a particular order for this measurement cross-section [32]. The second order perturbation theory in $H_{\text{p.e.}}$ leads to expectation values of the type

$$\Gamma_{k_1,k_2}(t_2, t_1; t_1', t_2') = \left\langle c_{k_2}^\dagger(t_2) c_{k_1}^\dagger(t_1) c_{k_1}(t_1') c_{k_2}(t_2') \right\rangle, \quad (5)$$

where the times are ordered such that $t_1 > t_2$ (see S.M. for a detailed derivation) and the spin indices are suppressed for clarity. Note that this is not a time-ordered expectation value, so the order of the operators remains fixed — the unprimed operators come after the primed. The total cross section includes the sum of Γ_{k_1,k_2} and the same term with the quasiparticle momenta exchanged, Γ_{k_2,k_1} .

A useful and intuitive way to visualize two-particle correlation functions G_2 (similar to Eq. 5) is diagrammatically, as shown in Fig. 2(a). A general vertex describing the propagation of two particles from $(1', 2')$ to $(1, 2)$ can be drawn with creation operators as lines coming out of the vertex, and annihilation operators as lines going in. They also dictate 4 external legs that then can undergo various complex processes in the shaded square. The power of such G_2 diagrams is that they directly describe scattering processes similar to the ones discussed within our paper. Within the shaded square region of the generic diagram, complex interactions can occur, highlighting the power of such G_2 diagrams to be adapted for directly describing various scattering processes, as detailed below.

Without introducing any further interactions (*e.g.* free electrons), and as long as momentum is a good quantum number, the only way to connect this diagram with bare fermion propagators is shown in Fig. 2(b). This yields a

simple factorized form

$$\Gamma_{k_1, k_2}(t_2, t_1; t_{1'}, t_{2'}) = \langle c_{k_2}^\dagger(t_2) c_{k_2}(t_{2'}) \rangle \langle c_{k_1}^\dagger(t_1) c_{k_1}(t_{1'}) \rangle \\ = -G_{k_2}^<(t_{2'}, t_2) G_{k_1}^<(t_{1'}, t_1). \quad (6)$$

This is just the product of two independent ARPES signals, which is a natural piece of the C-ARPES process but yields no additional information beyond standard ARPES: the lesser Green's function in frequency domain is simply related to the spectrum by the fluctuation-dissipation relation

$$G_k^<(\omega) = -2i n_F(\omega) \text{Im} G_k^R(\omega), \quad (7)$$

where $n_F(\omega)$ is the Fermi function. This result is also clear from the diagrammatic structure, which consists of two fully independent electron propagators [c.f. Fig. 2(b)]. This diagram and the corresponding term captures the background that arises from the two independent single-electron ARPES processes, and it is identified as the uncorrelated \mathcal{U}_2 signal. The additional diagrams we will consider are part of the correlation signal.

B. Interacting electrons

A more interesting case arises when an additional interaction is introduced; this is most easily handled in diagrammatic form. The first term that does not result in a renormalization of the independent single propagators is shown in Fig. 2(c), where a momentum q is transferred from one of the electrons to the other. For example, if the interaction is an unscreened Coulomb interaction H_C , this would correspond to a correlation function

$$\Gamma_{k_1, k_2}(t_2, t_1; t_{1'}, t_{2'}) = \int dt_3 \left\langle c_{k_2}^\dagger(t_2) c_{k_1}^\dagger(t_1) H_C(t_3) c_{k_1}(t_{1'}) c_{k_2}(t_{2'}) \right\rangle \quad (8)$$

$$H_C = \sum_{q\ell\ell'} V_q c_{\ell'-q}^\dagger c_{\ell+q}^\dagger c_\ell c_{\ell'}. \quad (9)$$

where the internal t_3 variable is understood to occur between external times. H_C is placed in the center the expression found in the previous section and with the assignment of $(1, 1', 2, 2')$ as the external legs due to the time-ordering of the integration limits in the full form. This example illustrates the use of C-ARPES for measuring interactions between electrons. The Wick contraction of Eq. 8 matches the momenta of the external electrons (k_1 and k_2 , which are experimentally determined) with the momenta involved in the interactions. In other words, the experiment probes the amplitude of the interaction V_q at $q = k_2 - k_1$.

This idea extends to dynamic interactions, *i.e.* that depend on both energy and momentum. Working in the limit of a long pulse — *i.e.* where the duration of the probe pulse is much longer than the characteristic time

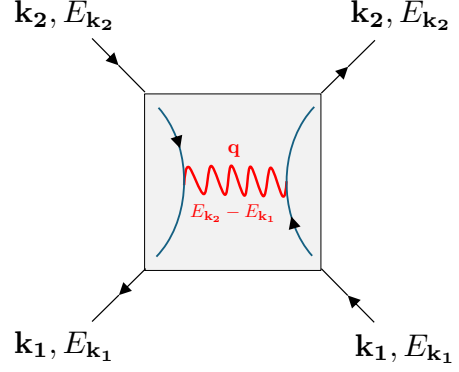


FIG. 3. Feynman diagram G_2 in energy and momentum space for the the C-ARPES scattering process with a single scattering event that transfers momentum q and energy $E_{k_1} - E_{k_2}$. The momenta and energies indicated are those of the photoemitted electrons measured by the C-ARPES experiment.

scale associated with the energies involved — we can effectively restore time translation invariance and can convert the time domain diagram of Fig. 2(c) into the frequency domain version shown in Fig. 3. A straightforward evaluation this diagram, which will appear as a correlation on top of the independent single electron ARPES processes, yields

$$C_2 = \left| G_{k_1}^<(E_{k_1}) G_{k_2}^<(E_{k_2}) \right|^2 \text{Re} [V_q(E_{k_2} - E_{k_1})] \delta_{q, k_2 - k_1} \quad (10)$$

for the C-ARPES vertex, thus enabling direct access to the interaction $V_q(\omega)$. Only the real part of $V_q(\omega)$ appears since the diagram is symmetric under the exchange of electrons, and the imaginary part of the interaction is anti-symmetric in energy. Note that in Eq. 10 the two electron momenta k_1 and k_2 , as well as the electron energies E_{k_1} and E_{k_2} , are free, but the signal will rapidly decay once the electrons are not on-shell, *e.g.* when E_{k_1} is not close to the electron dispersion $\varepsilon(k_1)$.

Interestingly, the structure of this diagram is quite close to that for RIXS where the interaction is mediated by a boson[17]. However, the added advantage of C-ARPES over RIXS is that, through the electron energy and momenta, one can directly interrogate the interaction of the (possibly effective) boson with specific electron states. This is not possible in the photon-in/photon-out setup of RIXS, where the signal is averaged over the entire Brillouin zone.

Peierls instability

In the following, we illustrate how C-ARPES can probe electron-electron interactions using the example of a CDW instability in 1D induced by the Kohn anomaly.

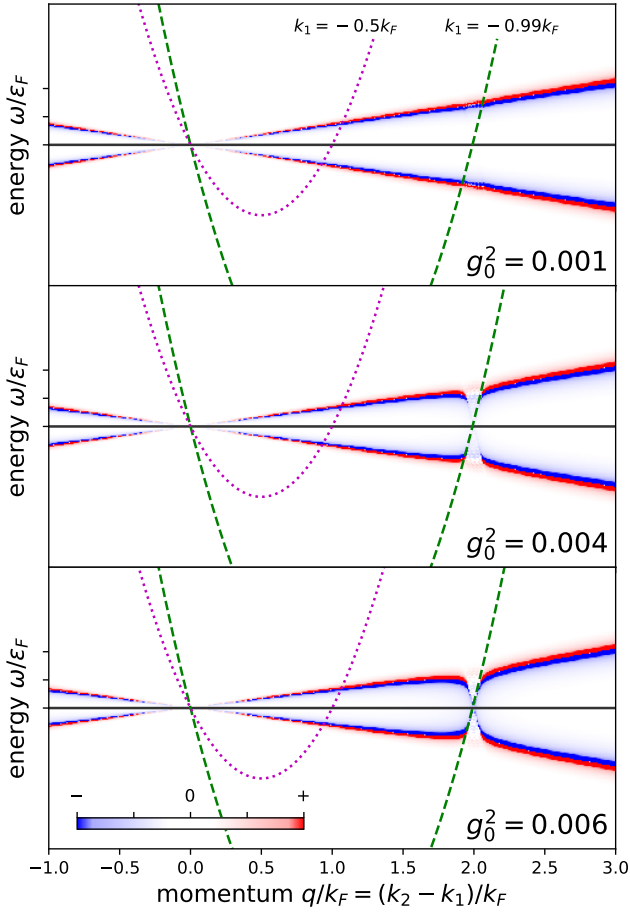


FIG. 4. Phonon-mediated electron-electron interaction $\text{Re}[V_q(\omega)]$ shown in false color. The dotted (dashed) line are the curves traced out in the $q = k_2 - k_1, \omega = E_2 - E_1$ plane obtained by fixing k_1 at the indicated value and varying k_2 with both energies $\varepsilon_{1,2}$ remaining on-shell [$E_{1,2} = \varepsilon(k_{1,2})$].

Specifically, we use a parabolic dispersion $\varepsilon(k) = k^2$ and a Fermi energy $\varepsilon_F = 1$. The nesting of the Fermi surface causes strong charge fluctuations at momenta $q = 2k_F$, where k_F is the Fermi wavevector; these fluctuations soften the phonons at the same momenta. In this case, the boson line in Fig. 3 is the renormalized phonon, and we can use C-ARPES to retrieve the phonon-mediated electron-electron interactions $V_q(\omega) = g_q^2 D_q(\omega)$. We use a deformation potential interaction vertex $g_q \sim |q|$ and an acoustic phonon with sound velocity c (S.M. section C provides details of the Kohn anomaly mechanism).

As the electron-phonon coupling strength g_0 increases, the peak in the charge susceptibility (Lindhard function) grows[36], and the phonon softens at $q = 2k_F$. Now, C-ARPES probes the real part of the interactions, displayed in Fig. 4 in false color, by picking out the two photoelectron momenta and energies. To illustrate how different sets of pairs (k_1, E_1) and (k_2, E_2) select the momentum and energy along which we measure V_q via C-ARPES we use non-interacting bands, which fix the en-

ergies to be equal to the on-shell energies [i.e. simply on the electron band $\varepsilon(k)$], so that the only two free variables are the photoelectron momenta k_1 and k_2 . We next pick $k_1 = -0.99k_F$ such that $\varepsilon(k_1)$ lies just below the Fermi level for left-moving electrons, and consider the C-ARPES signal as a function of k_2 . This traces out the dashed green curve shown in Fig. 4, and measures the electron-phonon interaction along this line. Choosing a different momentum such as $k_1 = -0.5k_F$ traces out a different slice of the interactions (dotted line).

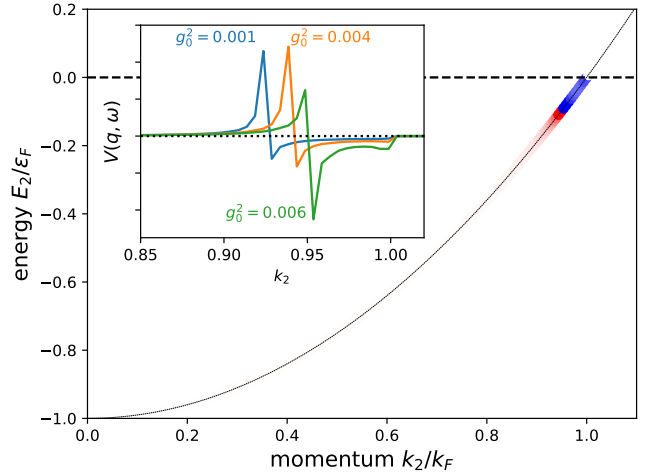


FIG. 5. Phonon mediated electron-electron interaction $V_q(\omega) = g_0^2 D_q(\omega)$ as measured with C-ARPES . The main panel shows the result of an experiment where $k_1 = -0.99k_F$, and k_2 is varied. A nonzero signal is only observed along the band dispersion (see text). Inset: Signal as measured along the band for various values of the coupling strength g_0 .

Fig. 5 displays the result of such an experiment, where we have fixed $k_1 = -0.99k_F$. The majority of the signal occurs when the second photoelectron is also emitted from near the Fermi level. Moreover, as the interaction strength g_0 increases the interaction $V_q(\omega)$ becomes more attractive (negative $\text{Re}[V_q(\omega)]$) which eventually leads to the formation of a CDW[37].

It is interesting to note that at $k_1 = -0.5k_F$, there is also a k_2 where a nonzero signal can be observed, even though this is not at the typical $q = 2k_F$ that is commonly associated with CDW formation in 1D. This can be seen in Fig. 4 where the dotted line intersects a non-zero part of $V_q(\omega)$ away from $\omega = 0$. The signal appears at $k_2 < 2k_F$, where the electron dispersion intersects with the sharp feature in the phonon-mediated interaction at $\Omega = E_2 - E_1 \approx cq$, where c is the sound velocity. In other words, C-ARPES can be employed to map the dispersion of the bosonic mode. This example clearly underscores the capability of C-ARPES in elucidating the interactions that ultimately give rise to the emergent CDW phase, demonstrating its potential to precisely identify the electrons involved in the process.

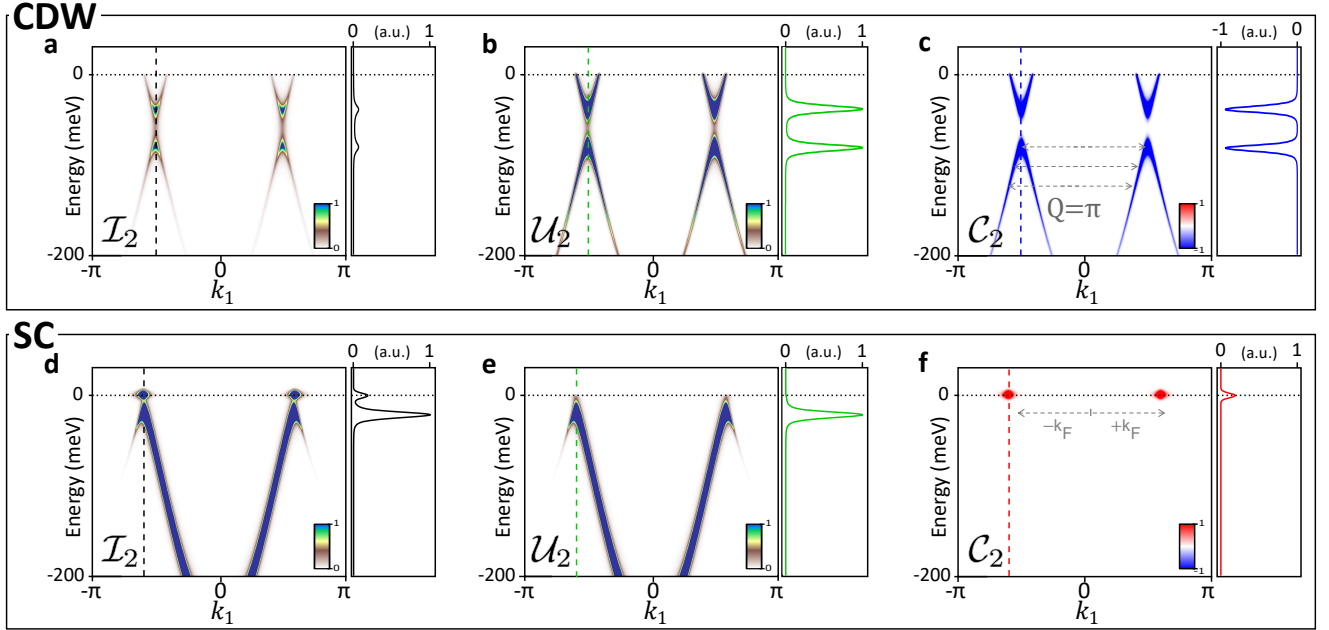


FIG. 6. Total coincidence signal (\mathcal{I}_2), uncorrelated background (\mathcal{U}_2), and C-ARPES intensity (\mathcal{C}_2), considering all possible electrons with momentum k_1 for a 1D CDW system, with $k_2 = k_1 + Q$ (a-c), and for a SC, with $k_2 = -k_1$ (d-f). Here we use $\Delta = 20$ meV for both CDW and SC gaps, and a broadening in energy of 5 meV is used. Energy distribution curves (on the right) are plotted to highlight the contribution of correlations to \mathcal{I}_2 .

C. Ordered Phases

Having discussed the extraction of dynamic electron interactions via C-ARPES, we present two key examples of the C-ARPES signal for ordered phases in 1D: CDW and superconductivity (SC). There are clear distinctions between the two cases, which can already be seen by considering the instantaneous correlations. For SC, Stahl et al.[32] show that for an ideal ultrashort pulse $\mathcal{C}_2 \propto |\langle c_{k\uparrow} c_{-k\downarrow} \rangle|^2$. For a CDW, a similar calculation yields $\mathcal{C}_2 \propto -|\langle c_k^\dagger c_{k+Q} \rangle|^2$, which has an opposite sign. This is a qualitative distinction that arises in addition to the momentum and energy structure that we discuss in this section.

1. Charge density wave

We consider the case of a simple CDW with wavevector Q that is described by an *anomalous* off-diagonal Green's function, such as $\langle c_{k+Q}^\dagger(t) c_k(t') \rangle$. With this possibility, the two points of non-equal momenta in the G_2 diagram can be directly connected with $k_2 = k + Q$. We can read off from the diagram of Fig. 2(d) that the C-ARPES correlation function, on top of the uncorrelated contribution \mathcal{U}_2 , is

$$\Gamma_{k_1, k_2} = \langle c_{k_1+Q}^\dagger(t_2) c_{k_1}(t_1') \rangle \langle c_{k_1}^\dagger(t_1) c_{k_1+Q}(t_2') \rangle \quad (11)$$

$$= -F_{k_1}^<(t_1', t_2) F_{k_1+Q}^<(t_2', t_1), \quad (12)$$

where F_{k_1} and F_{k_1+Q} denote the two off-diagonal components of the 2×2 Nambu Green's function \mathcal{G}_{k_1} . In the frequency domain, this becomes

$$\mathcal{C}_2 = -F_{k_1}^<(E_{k_1}) F_{k_1+Q}^<(E_{k_1+Q}) = -\left|F_{k_1}^<(E_{k_1})\right|^2 \quad (13)$$

having used the additional constraint that the photoelectron energies are equal, $E_{k_1} = E_{k_1+Q}$ (*i.e.*, static CDW order). We note that the same result can be obtained from straightforward perturbation theory, without referring to diagrams.

The retarded Green's function for a mean field CDW is

$$\mathcal{G}_k^R(\omega) = \frac{1}{(\omega - \xi_+ + i0^+) \tau_0 - \xi_- \tau_3 - \Delta \tau_1}. \quad (14)$$

Here, τ_i are the Pauli matrices, $\xi_\pm = \varepsilon(k) \pm \varepsilon(k+Q)$, where $\varepsilon(k)$ is the bare quasiparticle dispersion, and Δ is the CDW gap. The anomalous propagator F is the off-diagonal component of this matrix. Via the fluctuation-dissipation relation, the C-ARPES signal is then

$$\mathcal{C}_2 = -\left|2n_F(E_{k_1}) \text{Im} \frac{\Delta}{(E_{k_1} - \xi_+ + i0^+)^2 - (\xi_-^2 + \Delta^2)}\right|^2, \quad (15)$$

where n_F is the Fermi-Dirac distribution.

We now select the two photoelectrons to have the same energy ($E_{k_1} = E_{k_2}$), and fix their momenta to be separated by the CDW wavevector Q . In the non-interacting

limit, the four free variables ($k_1, k_2, E_{k_1}, E_{k_2}$) are reduced to just two by the relationships $k_2 = k_1 + Q$ and $E_{k_1} = E_{k_2}$, and in what follows we consider C-ARPES as a function of these two. In Fig. 6, in the top row, we show the results obtained for a 1D CDW system as a function of the remaining free variable k_1 and E_{k_1} for a mean field CDW with a finite chemical potential, which shifts the gap away from the Fermi level. Fig. 6c shows the C-ARPES intensity \mathcal{C}_2 , which is the difference between the coincidence signal \mathcal{I}_2 (panel a) and the uncorrelated single electron background \mathcal{U}_2 (panel b). We observe a strong negative C-ARPES intensity in the vicinity of the single particle spectral gap, some distance below the Fermi level. The energy distribution curve at k_1 , where the CDW gap opens, is plotted on the side of each panel and clearly highlights the strong suppression observed for the total coincidence intensity \mathcal{I}_2 , given by the negative \mathcal{C}_2 , if compared with the uncorrelated contribution \mathcal{U}_2 .

2. Superconductivity

The superconducting case has been already discussed in detail by Stahl et al.[32]. The key difference from the CDW case is that the time-ordered versions arise instead of occupied (lesser) Green's functions, which contain the square modulus of the imaginary part of the spectrum. This fact, together with the symmetric nature of the superconducting spectrum, limits the signal to only being visible near $E_k = E_{-k} \approx 0$ (see also Refs. [29, 38, 39]). The resulting C-ARPES signal for a 1D SC system is

$$\mathcal{C}_2 = \left| \frac{\Delta}{(\omega + i0^+)^2 - (\xi_k^2 + \Delta^2)} \right|^2 \cdot \delta(E_k + E_{-k}). \quad (16)$$

In Fig. 6, in the bottom row, \mathcal{C}_2 , \mathcal{I}_2 and \mathcal{U}_2 are evaluated in the case of a 1D BCS-like superconductor ($\Delta = 20\text{meV}$), for any possible k_1 electron interacting with a $k_2 = -k_1$ electron at the same energy. On the right side of panels d-f, the energy distribution curve at the Fermi wavevector is shown for direct evaluation of the C-ARPES intensity. The C-ARPES signal, \mathcal{C}_2 , is characterized by a peak at the Fermi energy that has no counterpart in the ARPES spectrum, demonstrating the potential of C-ARPES to explore the properties of correlated systems with unprecedented direct access to the two-electron correlation function with momentum resolution.

III. DISCUSSION

C-ARPES promises an unprecedented ability to untangle the otherwise averaged interactions by picking out specific electron pairs and examining their interactions. In this work, we have applied this to the investigation of a phonon-mediated effective electron-electron interaction, and we have just begun to lay the foundation

for the C-ARPES technique by considering mean-field CDW and SC orders in 1D, with the pairing function peaked at a singular wavevector and without energy dependence. However, C-ARPES could help us to go beyond our current understanding of quantum materials by directly studying the energy dependence of the effective pairing boson underlying different emergent phases, such as strong-coupling Eliashberg superconductors[40–42] and fluctuating charge density wave orders[7, 43, 44].

Within the context of charge density waves, there is uncertainty regarding the mechanism by which they are formed that could be addressed with C-ARPES. Specifically, both electron-lattice (Peierls) and electron-electron (Coulomb) interactions could give rise to charge density wave instabilities[45–47]. Both mechanisms involve the complex interplay of Fermi surface topology, momentum-dependence of the electron-phonon vertex[48], and other details that go into determining the effective interaction. For example, the random phase approximation (RPA), commonly employed to simulate and compare with scattering experiments, relies on both the polarizability function and the effective potential. The standard Lindhard equation for the polarizability involves summing over all possible electronic states. However, this approach often fails to quantitatively capture certain scattering experiments, possibly because it neglects an unknown vertex that weights the momenta that go into the calculation. Indeed, in strongly correlated systems with charge order, such as cuprate high- T_c superconductors, the RPA breaks down, as evidenced by momentum-resolved electron energy loss spectroscopy (M-EELS) and RIXS experiments [49–51].

In a similar manner to the approach discussed in Section II.B in the context of Peierls instabilities, C-ARPES could also be employed to resolve the $\Omega - q$ structure of bosonic modes in situations where they are inaccessible through direct scattering experiments. For example, also in the high- T_c cuprates there remains uncertainty about the nature of the dynamic correlations associated with this charge order. Based on anomalies observed in the RIXS-measured phonon line, an acoustic low-energy dispersion was proposed [52–54]. However, extending measurements beyond the high-symmetry directions of the Brillouin zone reveals a more intricate structure of dynamic charge order correlations, likely reflecting the effective form of the Coulomb interactions [7, 51, 55].

Finally, while the present study focused on the theoretical modeling of the C-ARPES signal, it is nonetheless essential to briefly address the relationship between the theoretical framework outlined herein and its practical experimental implementation. C-ARPES, akin to 2e-ARPES, relies on the coincident detection of two electrons, highlighting the need for a specialized coincidence electron detection setup. This may entail the implementation of two synchronized conventional single-hit electron detectors [24, 27, 28, 31] or a specialized multi-hit electron detector [56, 57].

In the specific case of C-ARPES, it is evident that the

temporal and spatial envelope of the UV beam should be of the order of the underlying Γ_{k_1, k_2} correlation length and time (for example, in conventional superconductors, these two are typically on the order of tens-to-hundreds of femtoseconds and nanometers, respectively). In scenarios where the temporal and spatial profiles of a UV pulse exceed the intrinsic coherence time and length of electron correlations and/or in the presence of non-ideal detection schemes and extrinsic background sources, the C_2 -signal-to-background ratio may decrease.

In experimental C-ARPES efforts, by continuously changing the temporal duration or the spot size of the UV beam, we will effectively separate the emergence of the C_2 signal from the underlying background. We believe that because of its favorable cross-section and direct access to Γ_{k_1, k_2} , rather than a higher order scattering process such as is involved in 2e-ARPES where a single photon is responsible for emitting two electrons [28, 29, 31, 38], C-ARPES has the potential to unravel the interactions into resolvable, understandable building blocks upon which theories can be constructed and tested.

AUTHOR CONTRIBUTIONS

AFK, EHdSN and FB conceived the original idea for the work. AFK and HL developed the theoretical framework of the CARPES response. FG contributed to the analysis of mean field CDW and SC order. FG, NG, EHdSN, and FB provided the experimental context. All authors contributed to the writing of the manuscript, and read and approved the final manuscript.

ACKNOWLEDGMENTS

We acknowledge helpful discussions with Steve Johnston. This research is funded by the Gordon and Betty Moore Foundation’s EPiQS Initiative, Grant GBMF12761 to F.B., A.F.K., and E.H.d.S.N. F.B. acknowledges support from the Natural Sciences and Engineering Research Council of Canada (NSERC), the Canada Research Chairs Program, the Canada Foundation for Innovation (CFI); the Fonds de recherche du Québec — Nature et Technologies (FRQNT), and the Ministère de l’Économie, de l’Innovation et de l’Énergie — Québec.

-
- [1] J. A. Sloboda, Y. He, and Z.-X. Shen, *Reviews of Modern Physics* **93**, 025006 (2021).
 - [2] F. Boschini, M. Zonno, and A. Damascelli, *Reviews of Modern Physics* **96**, 015003 (2024).
 - [3] T. P. Devereaux and R. Hackl, *Reviews of modern physics* **79**, 175 (2007).
 - [4] L. J. Ament, M. Van Veenendaal, T. P. Devereaux, J. P. Hill, and J. Van Den Brink, *Reviews of Modern Physics* **83**, 705 (2011).
 - [5] M. Mitrano, S. Johnston, Y.-J. Kim, and M. P. M. Dean, *Phys. Rev. X* **14**, 040501 (2024).
 - [6] F. M. F. de Groot, M. W. Havercort, H. Elnaggar, A. Juhin, K.-J. Zhou, and P. Glatzel, *Nature Reviews Methods Primers* **4**, 45 (2024).
 - [7] E. H. da Silva Neto, A. Frano, and F. Boschini, *Frontiers in Electronic Materials* **4** (2024), 10.3389/femat.2024.1473324.
 - [8] A. Lanzara, P. Bogdanov, X. Zhou, S. Kellar, D. Feng, E. Lu, T. Yoshida, H. Eisaki, A. Fujimori, K. Kishio, *et al.*, *Nature* **412**, 510 (2001).
 - [9] P. Johnson, T. Valla, A. Fedorov, Z. Yusof, B. Wells, Q. Li, A. Moodenbaugh, G. Gu, N. Koshizuka, C. Kendziora, *et al.*, *Physical Review Letters* **87**, 177007 (2001).
 - [10] W. Lee, S. Johnston, T. Devereaux, and Z.-X. Shen, *Physical Review B—Condensed Matter and Materials Physics* **75**, 195116 (2007).
 - [11] M. Zonno, F. Boschini, and A. Damascelli, *Journal of Electron Spectroscopy and Related Phenomena* **251**, 147091 (2021).
 - [12] H. Iwasawa, Y. Yoshida, I. Hase, K. Shimada, H. Namatame, M. Taniguchi, and Y. Aiura, *Scientific reports* **3**, 1930 (2013).
 - [13] K. Byczuk, M. Kollar, K. Held, Y.-F. Yang, I. Nekrasov, T. Pruschke, and D. Vollhardt, *Nature Physics* **3**, 168 (2007).
 - [14] F. Mazzola, J. W. Wells, R. Yakimova, S. Ulstrup, J. A. Miwa, R. Balog, M. Bianchi, M. Leandersson, J. Adell, P. Hofmann, and T. Balasubramanian, *Phys. Rev. Lett.* **111**, 216806 (2013).
 - [15] F. Boschini, E. da Silva Neto, E. Razzoli, M. Zonno, S. Peli, R. Day, M. Michiardi, M. Schneider, B. Zwartsenberg, P. Nigge, *et al.*, *Nature materials* **17**, 416 (2018).
 - [16] M. Na, A. K. Mills, F. Boschini, M. Michiardi, B. Nosarzewski, R. P. Day, E. Razzoli, A. Sheyerman, M. Schneider, G. Levy, *et al.*, *Science* **366**, 1231 (2019).
 - [17] T. Devereaux, A. Shvaika, K. Wu, K. Wohlfeld, C. Jia, Y. Wang, B. Moritz, L. Chaix, W.-S. Lee, Z.-X. Shen, *et al.*, *Physical Review X* **6**, 041019 (2016).
 - [18] C. D. Dashwood, A. Geondzhian, J. G. Vale, A. C. Pakpour-Tabrizi, C. A. Howard, Q. Faure, L. S. I. Veiga, D. Meyers, S. G. Chiuzbaian, A. Nicolaou, N. Jaouen, R. B. Jackman, A. Nag, M. García-Fernández, K.-J. Zhou, A. C. Walters, K. Gilmore, D. F. McMorrow, and M. P. M. Dean, *Phys. Rev. X* **11**, 041052 (2021).
 - [19] M. Zinouyeva, R. Heid, G. Merzoni, R. Arpaia, N. Andreev, M. Biagi, N. B. Brookes, D. Di Castro, A. Kalaboukhov, K. Kummer, F. Lombardi, L. Martinelli, F. Rosa, F. Yakhou-Harris, L. Braicovich, M. Moretti Sala, P. G. Radaelli, and G. Ghiringhelli, arXiv:2501.12089 (2025).
 - [20] F. Schumann, C. Winkler, G. Kerhervé, and J. Kirschner, *Physical Review B—Condensed Matter and Materials Physics* **73**, 041404 (2006).
 - [21] F. Schumann, C. Winkler, and J. Kirschner, *Physical review letters* **98**, 257604 (2007).

- [22] F. Schumann, C. Winkler, and J. Kirschner, *physica status solidi (b)* **246**, 1483 (2009).
- [23] M. Munoz-Navia, C. Winkler, R. Patel, M. Birke, F. Schumann, and J. Kirschner, *Journal of Physics: Condensed Matter* **21**, 355003 (2009).
- [24] M. Huth, C.-T. Chiang, A. Trützschler, F. O. Schumann, J. Kirschner, and W. Widdra, *Applied Physics Letters* **104** (2014).
- [25] I. Kostanovskiy, F. Schumann, Y. Aliaev, Z. Wei, and J. Kirschner, *Journal of Physics: Condensed Matter* **28**, 015601 (2015).
- [26] F. Schumann, Y. Aliaev, I. Kostanovskiy, G. Di Filippo, Z. Wei, and J. Kirschner, *Physical Review B* **93**, 235128 (2016).
- [27] A. Trützschler, M. Huth, C.-T. Chiang, R. Kamrla, F. O. Schumann, J. Kirschner, and W. Widdra, *Physical Review Letters* **118**, 136401 (2017).
- [28] C.-T. Chiang, A. Trützschler, M. Huth, R. Kamrla, F. O. Schumann, and W. Widdra, *Progress in Surface Science* **95**, 100572 (2020).
- [29] F. Mahmood, T. Devvereaux, P. Abbamonte, and D. K. Morr, *Physical Review B* **105**, 064515 (2022).
- [30] T. Leitner, A. Born, I. Bidermane, R. Ovsyannikov, F. O. Johansson, Y. Sassa, A. Föhlisch, A. Lindblad, F. Schumann, S. Svensson, *et al.*, *Journal of Electron Spectroscopy and Related Phenomena* **250**, 147075 (2021).
- [31] J. Zwettler, H. Amir, F. H. Marashi, N. Bielinski, S. Patel, P. Mahaadev, Y. Huang, D. Chaudhuri, X. Guo, T. C. Chiang, *et al.*, *Journal of Electron Spectroscopy and Related Phenomena* **270**, 147417 (2024).
- [32] C. Stahl and M. Eckstein, *Physical Review B* **99**, 241111 (2019).
- [33] G. D. Mahan, *Many Particle Physics* (Springer, New York, NY10013, USA, 2010).
- [34] H. Bruus and K. Flensberg, *Many-body quantum theory in condensed matter physics: an introduction* (OUP Oxford, 2004).
- [35] A. Damascelli, Z. Hussain, and Z.-X. Shen, *Reviews of modern physics* **75**, 473 (2003).
- [36] B. Mihaila, arXiv preprint arXiv:1111.5337 (2011).
- [37] G. Grüner, *Reviews of modern physics* **60**, 1129 (1988).
- [38] T. P. Devvereaux, M. Claassen, X.-X. Huang, M. Zaletel, J. E. Moore, D. Morr, F. Mahmood, P. Abbamonte, and Z.-X. Shen, *Physical Review B* **108**, 165134 (2023).
- [39] Y. Su and C. Zhang, *Physical Review B* **101**, 205110 (2020).
- [40] G. Eliashberg, *Sov. Phys. JETP* **11**, 696 (1960).
- [41] D. Scalapino, J. Schrieffer, and J. Wilkins, *Physical Review* **148**, 263 (1966).
- [42] A. Abrikosov, L. Gor'Kov, and I. Dzyaloshinskii, *Physics* (Pergamon Press, New York, 1965) (1965).
- [43] S. A. Kivelson, I. P. Bindloss, E. Fradkin, V. Oganesyan, J. Tranquada, A. Kapitulnik, and C. Howald, *Reviews of Modern Physics* **75**, 1201 (2003).
- [44] S. Wandel, F. Boschini, E. da Silva Neto, L. Shen, M. Na, S. Zohar, Y. Wang, S. Welch, M. Seaberg, J. Koralek, *et al.*, *Science* **376**, 860 (2022).
- [45] K. Rossnagel, *Journal of Physics: Condensed Matter* **23**, 213001 (2011).
- [46] H. Watanabe, K. Seki, and S. Yunoki, *Physical Review B* **91**, 205135 (2015).
- [47] E. G. van Loon, M. Rösner, G. Schönhoff, M. I. Katsnelson, and T. O. Wehling, *npj Quantum Materials* **3**, 32 (2018).
- [48] H.-M. Eiter, M. Lavagnini, R. Hackl, E. A. Nowadnick, A. F. Kemper, T. P. Devvereaux, J.-H. Chu, J. G. Analytis, I. R. Fisher, and L. Degiorgi, *Proceedings of the National Academy of Sciences* **110**, 64 (2013).
- [49] M. Mitrano, A. A. Husain, S. Vig, A. Kogar, M. S. Rak, S. I. Rubeck, J. Schmalian, B. Uchoa, J. Schneeloch, R. Zhong, G. D. Gu, and P. Abbamonte, *Proceedings of the National Academy of Sciences* **115**, 5392 (2018).
- [50] A. A. Husain, M. Mitrano, M. S. Rak, S. Rubeck, B. Uchoa, K. March, C. Dwyer, J. Schneeloch, R. Zhong, G. D. Gu, and P. Abbamonte, *Phys. Rev. X* **9**, 041062 (2019).
- [51] F. Boschini, M. Minola, R. Sutarto, E. Schierle, M. Bluschke, S. Das, Y. Yang, M. Michiardi, Y. C. Shao, X. Feng, S. Ono, R. D. Zhong, J. A. Schneeloch, G. D. Gu, E. Weschke, F. He, Y. D. Chuang, B. Keimer, A. Damascelli, A. Frano, and E. H. da Silva Neto, *Nature Communications* **12** (2021), 10.1038/s41467-020-20824-7.
- [52] L. Chaix, G. Ghiringhelli, Y. Y. Peng, M. Hashimoto, B. Moritz, K. Kummer, N. B. Brookes, Y. He, S. Chen, S. Ishida, Y. Yoshida, H. Eisaki, M. Salluzzo, L. Braicovich, Z.-X. Shen, T. P. Devvereaux, and W.-S. Lee, *Nature Physics* **13**, 952 (2017).
- [53] J. Li, A. Nag, J. Pelliciari, H. Robarts, A. Walters, M. Garcia-Fernandez, H. Eisaki, D. Song, H. Ding, S. Johnston, R. Comin, and K.-J. Zhou, *Proceedings of the National Academy of Sciences* **117**, 16219 (2020).
- [54] W. S. Lee, K.-J. Zhou, M. Hepting, J. Li, A. Nag, A. C. Walters, M. Garcia-Fernandez, H. C. Robarts, M. Hashimoto, H. Lu, B. Nosarzewski, D. Song, H. Eisaki, Z. X. Shen, B. Moritz, J. Zaanen, and T. P. Devvereaux, *Nature Physics* **17**, 53–57 (2020).
- [55] K. Scott, E. Kisiel, T. J. Boyle, R. Basak, G. Jarrot, S. Das, S. Agrestini, M. Garcia-Fernandez, J. Choi, J. Pelliciari, J. Li, Y.-D. Chuang, R. Zhong, J. A. Schneeloch, G. Gu, F. Légaré, A. F. Kemper, K.-J. Zhou, V. Bisogni, S. Blanco-Canosa, A. Frano, F. Boschini, and E. H. da Silva Neto, *Science Advances* **9**, eadg3710 (2023).
- [56] R. Wallauer, S. Voss, L. Foucar, T. Bauer, D. Schneider, J. Titze, B. Ulrich, K. Kreidi, N. Neumann, T. Havermeier, *et al.*, *Review of Scientific Instruments* **83** (2012).
- [57] S. Voss, M. Tia, S. Schößler, A. Czasch, and O. Jagutzki, *Journal of Electron Spectroscopy and Related Phenomena* **241**, 146875 (2020).

Appendix A: Technical details

In this section, we derive the diagrammatic representation of the C-ARPES process. We begin from the expression obtained by Stahl et al.[32] (who termed it noise-correlation ARPES) for the 2-particle signal \mathcal{I}_2 . Note that here we explicitly distinguish between the ejected photoelectron momenta (denoted with p) and the quasiparticle momenta (denoted with k).

$$\begin{aligned} \mathcal{I}_2 = & \sum_{\substack{k_1, k_2, k_1', k_2' \\ \sigma_1, \sigma_2, \sigma_1', \sigma_2'}} \int_{-\infty}^{\infty} dt_1 \int_{-\infty}^{t_1} dt_2 \int_{-\infty}^{\infty} dt_{1'} \int_{-\infty}^{t_{1'}} dt_{2'} S(t_1)^* S(t_2)^* S(t_{1'}) S(t_{2'}) e^{-i\Omega(t_{1'}+t_{2'}-t_1-t_2)} \\ & \times \left[(M_{k_1, p'}^{\sigma_1, \tau'})^* (M_{k_2, p}^{\sigma_2, \tau})^* M_{k_2', p'}^{\sigma_2', \tau} M_{k_1', p'}^{\sigma_1', \tau'} \langle c^\dagger(2)c^\dagger(1)c(1')c(2') \rangle_0^c e^{-iE_p(t_2-t_{2'})} e^{-iE_{p'}(t_1-t_{1'})} \right. \\ & + (M_{k_1, p}^{\sigma_1, \tau})^* (M_{k_2, p'}^{\sigma_2, \tau'})^* M_{k_2', p'}^{\sigma_2', \tau'} M_{k_1', p}^{\sigma_1', \tau} \langle c^\dagger(2)c^\dagger(1)c(1')c(2') \rangle_0^c e^{-iE_p(t_1-t_{1'})} e^{-iE_{p'}(t_2-t_{2'})} \\ & - (M_{k_1, p'}^{\sigma_1, \tau'})^* (M_{k_2, p}^{\sigma_2, \tau})^* M_{k_2', p'}^{\sigma_2', \tau'} M_{k_1', p'}^{\sigma_1', \tau} \langle c^\dagger(2)c^\dagger(1)c(1')c(2') \rangle_0^c e^{-iE_p(t_2-t_{1'})} e^{-iE_{p'}(t_1-t_{2'})} \\ & \left. - (M_{k_1, p}^{\sigma_1, \tau})^* (M_{k_2, p'}^{\sigma_2, \tau'})^* M_{k_2', p}^{\sigma_2', \tau} M_{k_1', p'}^{\sigma_1', \tau'} \langle c^\dagger(2)c^\dagger(1)c(1')c(2') \rangle_0^c e^{-iE_p(t_1-t_{2'})} e^{-iE_{p'}(t_2-t_{1'})} \right]. \end{aligned} \quad (\text{A1})$$

Note that here, $1 = (t_1, k_1, \sigma_1)$. The $S(t)$ functions are shape functions that are set by the probe profile; the $M_{k, p}^{\sigma, \tau}$ factors indicate the photoemission matrix element for a quasiparticle with momentum k and spin σ becoming a free electron with momentum p and spin τ ; E_p denotes the energy of the free photoemitted electron with momentum p . In what follows, we will suppress the spin indices — these can be straightforwardly restored. We will also assume the matrix elements conserve spin and momentum, i.e. $M_{k, p}^{\sigma, \tau} = M \delta_{\sigma, \tau} \delta_{k, p}$.

Eq. A1 can be significantly simplified by making two observations. First: the first and second lines are identical under the exchange of the free electron momenta $p \leftrightarrow p'$ (even without the matrix element simplification), and the same holds for the third and fourth lines. This yields

$$\begin{aligned} \mathcal{I}_2 = & |M|^4 \int_{-\infty}^{\infty} dt_1 \int_{-\infty}^{t_1} dt_2 \int_{-\infty}^{\infty} dt_{1'} \int_{-\infty}^{t_{1'}} dt_{2'} S(t_1)^* S(t_2)^* S(t_{1'}) S(t_{2'}) e^{-i\Omega(t_{1'}+t_{2'}-t_1-t_2)} \\ & \times \left[\left\langle c_p^\dagger(t_2) c_{p'}^\dagger(t_1) c_{p'}(t_{1'}) c_p(t_{2'}) \right\rangle_0^c e^{-iE_p(t_2-t_{2'})} e^{-iE_{p'}(t_1-t_{1'})} \right. \\ & \left. - \left\langle c_p^\dagger(t_2) c_{p'}^\dagger(t_1) c_p(t_{1'}) c_{p'}(t_{2'}) \right\rangle_0^c e^{-iE_p(t_2-t_{1'})} e^{-iE_{p'}(t_1-t_{2'})} \right] \\ & + p \leftrightarrow p' \end{aligned} \quad (\text{A2})$$

where we have explicitly denoted the time and momentum arguments. Our second observation is that we can exchange the dummy arguments $t_{1'}$ and $t_{2'}$ in the second line, and restore their ordering by swapping the operators,

$$\begin{aligned} \mathcal{I}_2 = & |M|^4 \int_{-\infty}^{\infty} dt_1 \int_{-\infty}^{t_1} dt_2 \int_{-\infty}^{\infty} dt_{1'} \int_{-\infty}^{\infty} dt_{2'} S(t_1)^* S(t_2)^* S(t_{1'}) S(t_{2'}) e^{-i\Omega(t_{1'}+t_{2'}-t_1-t_2)} \\ & \times \left\langle c_p^\dagger(t_2) c_{p'}^\dagger(t_1) c_{p'}(t_{1'}) c_p(t_{2'}) \right\rangle_0^c e^{-iE_p(t_2-t_{2'})} e^{-iE_{p'}(t_1-t_{1'})} \\ & + p \leftrightarrow p' \end{aligned} \quad (\text{A3})$$

Note that the upper limit of the $t_{2'}$ integration is now extended to ∞ . In what follows, we will make use of a general vertex $\Gamma_{p, p'}(t_2, t_1; t_{1'}, t_{2'})$, or in the frequency domain, $\tilde{\Gamma}_{p, p'}(\alpha_2, \alpha_1; \alpha_{1'}, \alpha_{2'})$, represented by Fig. 2 which we reproduce in Fig. S1 with slight modification to match the notation. With this, we can express \mathcal{I}_2 as

$$\begin{aligned} \mathcal{I}_2 = & |M|^4 \int_{-\infty}^{\infty} dt_1 \int_{-\infty}^{t_1} dt_2 \int_{-\infty}^{\infty} dt_{1'} \int_{-\infty}^{\infty} dt_{2'} S(t_1)^* S(t_2)^* S(t_{1'}) S(t_{2'}) e^{-i\Omega(t_{1'}+t_{2'}-t_1-t_2)} \\ & \times \Gamma_{p, p'}(t_2, t_1; t_{1'}, t_{2'}) \cdot e^{-iE_p(t_2-t_{2'})} e^{-iE_{p'}(t_1-t_{1'})} \\ & + p \leftrightarrow p' \end{aligned} \quad (\text{A4})$$

$$\begin{aligned} \mathcal{I}_2 = & |M|^4 \int_{-\infty}^{\infty} dt_1 \int_{-\infty}^{t_1} dt_2 \int_{-\infty}^{\infty} dt_{1'} \int_{-\infty}^{\infty} dt_{2'} S(t_1)^* S(t_2)^* S(t_{1'}) S(t_{2'}) e^{-i\Omega(t_{1'}+t_{2'}-t_1-t_2)} \\ & \times \left[\int d\alpha_1 d\alpha_2 d\alpha_{1'} d\alpha_{2'} \Gamma_{p, p'}(\alpha_2, \alpha_1; \alpha_{1'}, \alpha_{2'}) e^{i\alpha_2 t_2} e^{i\alpha_1 t_1} e^{-i\alpha_{2'} t_{2'}} e^{-i\alpha_{1'} t_{1'}} \right] \cdot e^{-iE_p(t_2-t_{2'})} e^{-iE_{p'}(t_1-t_{1'})} \\ & + p \leftrightarrow p' \end{aligned} \quad (\text{A5})$$

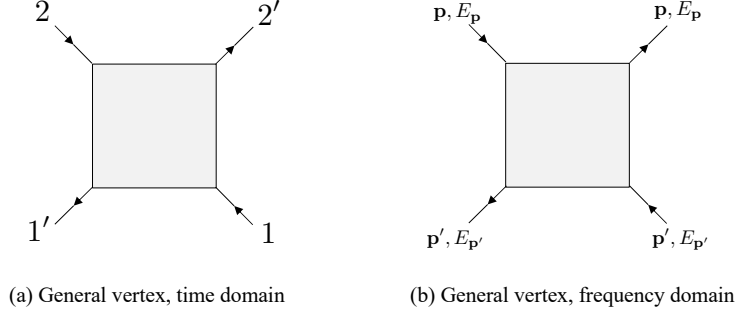


FIG. S1. Feynman diagram illustrating the 4-point vertex for the scattering process, where the primed (nonprimed) times and 4-momenta correspond to creation (annihilation) operators and have been drawn as outgoing (incoming) lines.

where we have implicitly used time-translation invariance to express the vertex in the frequency domain. We can work out the frequency (time) integrals over the α (t) variables; the shape functions here are used to regularize the Fourier integrals, and we will take the limit of $S(t) \rightarrow 1$ at the end. We find

$$\begin{aligned} \mathcal{I}_2 &= \frac{|M|^4}{2} \int d\alpha_1 d\alpha_2 d\alpha_{1'} d\alpha_{2'} \Gamma_{p,p'}(\alpha_2, \alpha_1; \alpha_{1'}, \alpha_{2'}) \\ &\quad \times \delta(E_p - \Omega - \alpha_{1'}) \cdot \delta(E_{p'} - \Omega - \alpha_{2'}) \\ &\quad \times \delta[\alpha_1 + \alpha_2 - \alpha_{1'} - \alpha_{2'}] \cdot \delta[(\alpha_1 - \alpha_2) - (E_p - E_{p'})]. \\ &\quad + p \leftrightarrow p' \end{aligned} \quad (\text{A6})$$

$$\begin{aligned} &= \frac{|M|^4}{2} \Gamma_{p,p'}(E_{p'} - \Omega, E_p - \Omega; E_p - \Omega, E_{p'} - \Omega) \\ &\quad + p \leftrightarrow p' \end{aligned} \quad (\text{A7})$$

In Eq. A6, the first set of delta functions indicates the relationship between the energy entering the diagram from the photon and photoemitted electron and the internal variables; the second set speaks to energy conservation within the diagram. Finally, we can measure the photoelectron energies $E_{p,p'}$ with respect to the photon energy, shifting them $E_{p,p'} - \Omega \rightarrow E_{p,p'}$. The resulting frequency domain vertex is shown in Fig. S1.

Appendix B: \mathcal{I}_2 for superconductivity

The case for superconductivity was worked out by Stahl et al.[32]. Here, it is convenient to re-arrange the terms in Eq. A1 somewhat differently, leading to

$$\begin{aligned} \mathcal{I}_2 &= |M|^4 \int_{-\infty}^{\infty} dt_1 \int_{-\infty}^{\infty} dt_2 \int_{-\infty}^{\infty} dt_{1'} \int_{-\infty}^{\infty} dt_{2'} S(t_1)^* S(t_2)^* S(t_{1'}) S(t_{2'}) e^{-i\Omega(t_{1'}+t_{2'}-t_1-t_2)} \\ &\quad \times \left\langle T_{\bar{t}}[c_p^\dagger(t_2)c_{p'}^\dagger(t_1)]T_t[c_{p'}(t_{1'})c_p(t_{2'})]\right\rangle_0^c e^{-iE_p(t_2-t_{2'})} e^{-iE_{p'}(t_1-t_{1'})} \\ &\quad + p \leftrightarrow p' \end{aligned} \quad (\text{B1})$$

where T_t ($T_{\bar{t}}$) denotes time-ordering (anti-time ordering) of the terms in brackets. Performing a Wick contraction yields for the anomalous term

$$\begin{aligned} \mathcal{I}_2 &= |M|^4 \int_{-\infty}^{\infty} dt_1 \int_{-\infty}^{\infty} dt_2 \int_{-\infty}^{\infty} dt_{1'} \int_{-\infty}^{\infty} dt_{2'} S(t_1)^* S(t_2)^* S(t_{1'}) S(t_{2'}) e^{-i\Omega(t_{1'}+t_{2'}-t_1-t_2)} \\ &\quad \times (F_p^\dagger)^{\bar{t}}(t_2 - t_1)(F_p)^t(t'_2 - t'_1) e^{-iE_p(t_2-t_{2'})} e^{-iE_{-p}(t_1-t_{1'})} \\ &\quad + p \leftrightarrow p' \end{aligned} \quad (\text{B2})$$

Appendix C: Phonon mediated electron-electron scattering

In Sec. II B, we illustrate the use of C-ARPES for measuring the interaction between electrons with the example of phonon-mediated scattering; in this section, we provide some additional details, which can be found in standard many-body theory textbooks[33, 34]. We consider the interaction between electrons and phonons for a single longitudinal acoustic phonon in 1D

$$H_{\text{ep}} = \frac{1}{\sqrt{V}} \sum_{qk} g_q c_{k+q}^\dagger c_k \left[a_q + a_{-q}^\dagger \right], \quad (\text{C1})$$

$$g_q = g_0 \frac{|q|^2}{\Omega_q}, \quad (\text{C2})$$

$$\Omega_q = c|q|. \quad (\text{C3})$$

In metals, phonons exhibit the Kohn anomaly, where there is a divergent response of the electron polarization $\Pi(q, \omega)$ at a momentum $q = 2k_F$. This quantity enters the phonon propagator via the Dyson equation

$$D(q, \omega) = \frac{2\Omega_q}{\omega^2 - \Omega_q^2 - 2\Omega_q g_q^2 \Pi(q, \omega)}, \quad (\text{C4})$$

and leads to a softening of the phonon at that momentum as shown in Fig. S2 where we plot the phonon spectral function. As the electron-phonon coupling is increased, a sharp dip develops in the phonon frequency, which eventually nears zero. This is a mechanism for the formation of a charge density wave (CDW), but in this section we will remain in the disordered phase.

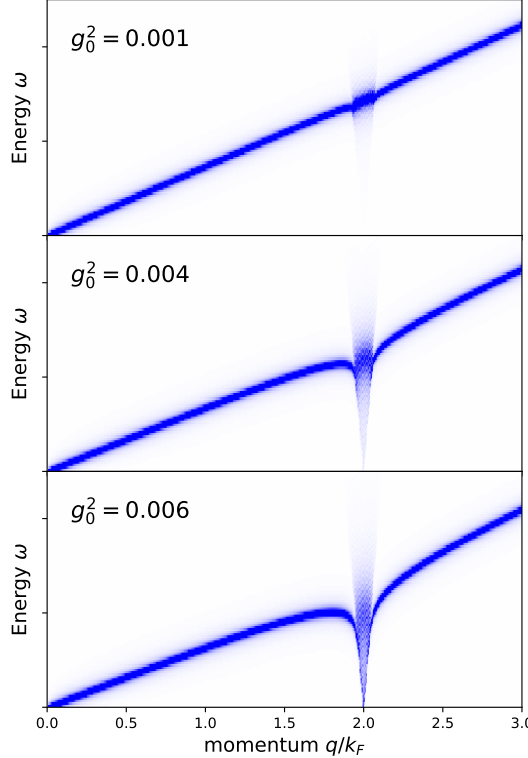


FIG. S2. Phonon spectral function $(-1/\pi)\text{Im}D(q, \omega)$ showing the development of the Kohn anomaly at $q = 2k_F$.

In turn, the electron-electron interaction is

$$V_q(\omega) = |g_q|^2 D(q, \omega). \quad (\text{C5})$$

We evaluate the polarizability $\Pi(q, \omega)$ for the electrons using the Lindhard formula[36], i.e. the bare bubble.